ELSEVIER

Seepage driving effect on deformations of San Fernando dams

Xiang Song Li[a,*], Haiyan Ming[1,b]

[a]*Department of Civil Engineering, Hong Kong University of Science and Technology, Clear Water Bay, Kowloon, Hong Kong, China*
[b]*Department of Civil Engineering, Shenzhen University, Shenzhen, China*

Abstract

In the process of flow deformation of an earth dam, the seepage force inside the dam plays a role as a driving force. The seepage force acts just like the gravitational force in terms of pushing soils away from their original locations after liquefaction is triggered. This paper draws attention to this seepage driving effect by presenting a set of fully coupled finite element analyses on the well-known San Fernando dams, with the objective of evaluating the impact of this seepage effect. The results indicate that while this effect is always there, its practical significance depends on a number of factors. In the case of the upper San Fernando dam, which experienced a significant, but restricted, downstream movement during the 1971 earthquake, the seepage driving effect was indeed significant. On the contrary, for the lower dam, which failed and slid into the upstream reservoir during the same earthquake, this seepage effect was relatively less pronounced. The detailed results of the analyses reveal the likely mechanisms of failure and deformation of the two dams and the likely cause behind the difference between their responses during the earthquake.
© 2004 Elsevier Ltd. All rights reserved.

Keywords: Flow deformation; Fully coupled analysis; Liquefaction; Residual strength; Seepage force; San Fernando dam

1. Introduction

It is the basic concept of flow liquefaction that when the driving shear stress on a potential slip surface through a liquefiable material is greater than its residual strength, the soil mass will move after liquefaction is triggered until a new equilibrium is established. The more the driving stress exceeds the residual strength, the greater the deformation and displacement may develop. Clearly, post-liquefaction flow deformations and displacements are sensitive to the residual strength of the soil as well as to the driving stress acting on it. Hence, uncertainties involved in both the driving stress and the residual strength may lead to an inaccurate evaluation and, consequently, inconsistent conclusions.

The seepage force is one of the driving forces acting on the soil skeleton, which plays the same role as the gravitational force in terms of driving soils away from their original positions upon liquefaction. While this effect is supposedly included in approximate ways in some popular procedures used in practice [1,2] and is naturally built in all fully coupled effective stress procedures [3–5], it has not been explicitly and cautiously examined in the past; and consequently, its impact on the extent of flow deformation and the underlying mechanics are not addressed.

In principle, for seepage driving force to be an important factor of post-liquefaction displacements, it must be significant, compared with gravitational driving force, and is present in loose liquefiable soils. Therefore, any analysis aimed at evaluating this seepage effect must correctly establish the field of seepage force in the dam under consideration and appropriately model the responses of liquefiable soils throughout the earthquake. As mentioned earlier, this seepage driving effect is naturally integrated in the basic formulation of a fully coupled effective stress procedure. However, for such a procedure to be effective in simulating the seepage induced post-liquefaction deformation, the constitutive model (or models) adopted must be

---

* Corresponding author. Tel.: +852-2358-7177; fax: +852-2358-1534.
E-mail address: xsli@ust.hk (X.S. Li).
[1] Formerly, Department of Civil Engineering, Hong Kong University of Science and Technology, Hong Kong, China.

able to realistically describe the stress–strain–strength behavior of the soils in the dam over the full range of loading conditions encountered, including the responses before and after liquefaction is triggered; for liquefied soils, the responses of flow liquefaction and cyclic mobility.

This paper presents a set of fully coupled finite element analyses on both the upper and lower San Fernando dams. The objectives of the analyses include (i) to evaluate the impact of the seepage force on the post-liquefaction deformation; and (ii) to show the possible mechanisms that made the responses of the two dams different during the 1971 earthquake. In particular, the upper San Fernando dam experienced a significant, but limited, deformation during that earthquake. Quantifying the deformation in such a category has its value in assessing the seismic performance of an embankment dam. By comparing the results with and without the seepage driving forces, one can see that the seepage driving effect in the upper San Fernando dam case is indeed significant and must be appropriately taken into account in performance evaluation and back analysis.

2. Numerical procedure

The numerical procedure used in the analyses is SUMDES2D [6], a two-dimensional finite element code. This procedure is a fully coupled effective-stress procedure [3–5] formulated based on the physical laws of balance of linear momentum and conservation of mass.

In order to simulate various soil behavior during earthquakes in a unified manner, a newly developed critical state bounding surface sand model [7] is plugged into the procedure. The unique feature of the model is that it incorporates the concept of state-dependent dilatancy [8] into its formulation. The constitutive model is supposed to describe with an acceptable accuracy the soil behavior over the full range of soil densities and loading conditions encountered. By adopting such a simulative constitutive model, the fully coupled numerical procedure can generate not only the global responses of an earth dam being analyzed, such as displacement, velocity, acceleration, as well as excess pore water pressure, but also soil responses such as stress and strain histories at specified locations throughout the dam. The global response of an earth dam can thus be traced back to the local material responses, making such a procedure a rather rational tool to investigate the seismic performance of earth dams and to help gaining in-depth understanding of the underlying mechanisms of the seepage effects on flow deformation.

The same numerical procedure and the same constitutive model were used to analyze the failure and remediation of the lower San Fernando dam [9]. The results of the analyses identified possible failure mechanisms of the embankment and effective remedial measures to improve the seismic performance of that dam.

3. Seepage driving force

In a saturated soil, solid particles are surrounded by pore fluid. The forces acting on a particle include the inter-granular contact forces, described through the effective stress σ'_{ij}, and that resulting from the pore pressure $u_w\delta_{ij}$, where δ_{ij} is the Kronecker delta. This can be illustrated by Fig. 1(a), the free body diagram of a sectioned particle (the shaded one in the figure). For clarity of illustration, it is assumed that the particle is subjected only to one-dimensional forces and the body force of the particle in the given direction is ignored. Note that, while the contact forces between particles are solely transferred through the solids, the pore pressure on the gross cross section of the soil is shared by the solids and the pore fluid, according to their proportions in the cross sectional area. The area proportions occupied by the solids and the pore fluid are presumably the same as their volumetric fractions, $(1-n)$ and n, respectively, where n is the porosity. This treatment implicitly assumes that the voids are isotropically distributed in soil.

Fig. 1(b) shows a continuum representation of the soil skeleton, in which $f\mathrm{d}x$ represents the forces exerted by the pore fluid due to seepage flow. In the absence of a global body force in the x-direction, the equilibrium of soil mass as a whole yields

$$\sigma'_x + u_{w,x} = 0 \tag{1}$$

where σ' denotes the effective stress in x-direction and u_w is the pore pressure. The equilibrium condition for the solid phase alone, as shown in Fig. 1(b), gives

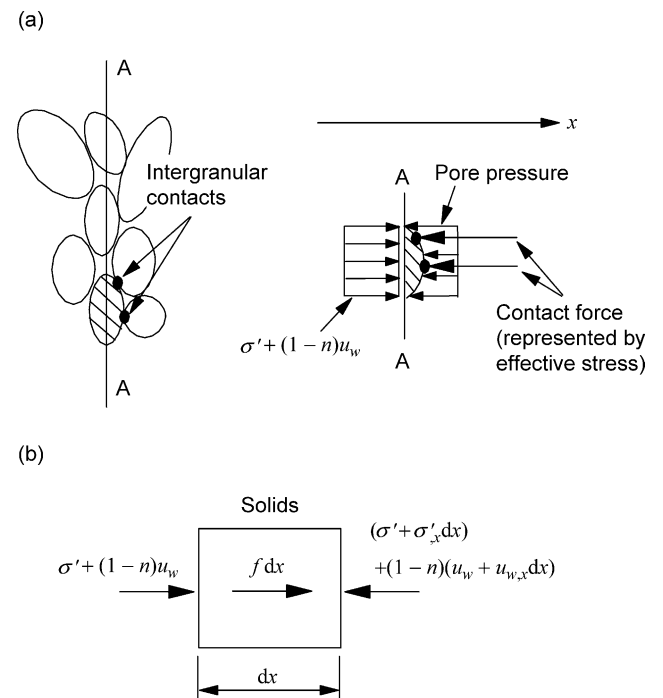$$f = \sigma'_x + (1-n)u_{w,x} \tag{2}$$

(a)

(b)

Fig. 1. Illustration of the force system acting on soil skeleton.

Combining Eqs. (1) and (2) yields

$$f = -nu_{w,x} \tag{3}$$

If the elevation head vanishes in the given direction, one has $\partial u_w / \partial x = -\gamma_w i$, where γ_w is the unit weight of the pore fluid and i is the hydraulic gradient. Hence,

$$f = n\gamma_w i \tag{4}$$

This is the per-unit-volume seepage-induced force acting on the soil skeleton. Because it is proportional to the volume of soil, this seepage force can be viewed as a body force acting on the solid phase. In the general three-dimensional cases involving dynamic effects, this per-unit-volume body force becomes a vector and can be written as

$$f_i = n[\rho_w(b_i - \ddot{u}_i) - u_{w,i}] \tag{5}$$

where the subscript i denotes the direction, ρ_w is the mass density of the pore fluid, b_i and u_i are the global body force function and the displacement, respectively. The superposed dots represent derivatives with respect to time. This force drives soil away from its original position upon liquefaction.
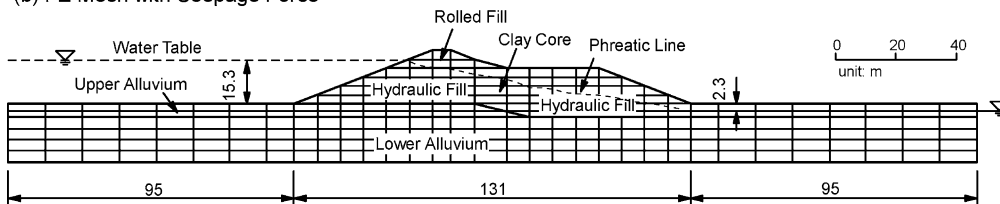
4. Finite element model of upper San Fernando dam

The finite element model for the lower San Fernando dam has been described in Ming and Li [9]. The same approach was used to set up the model for the upper San Fernando dam.

A typical cross-section of the upper San Fernando dam is illustrated in Fig. 2(a), and Fig. 2(b) and (c) show the finite element mesh of the dam used in this study. The corrected
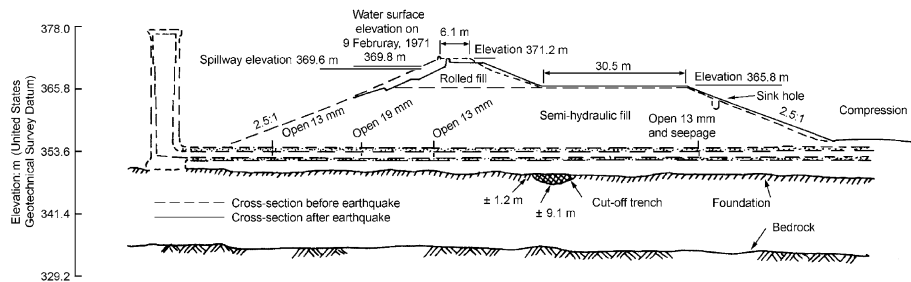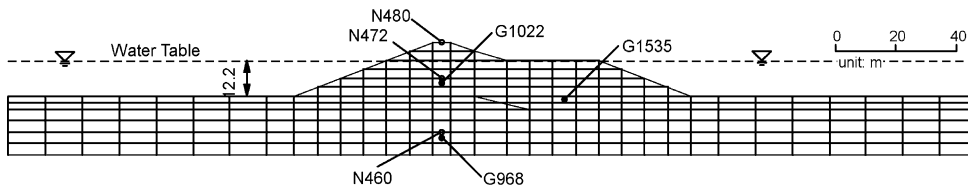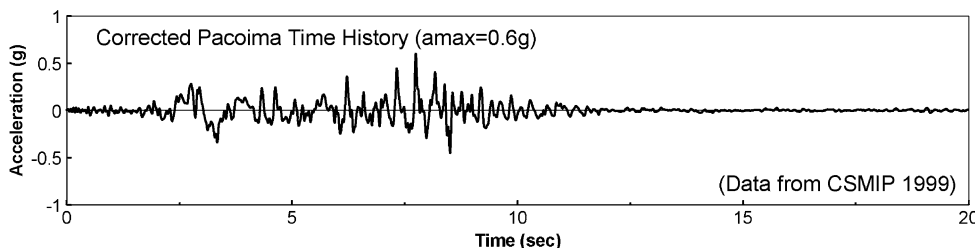

Fig. 2. Typical cross-section of the upper San Fernando dam and the finite element meshes used in analyses.

Pacoima accelerogram [10] scaled to a peak acceleration of 0.6 g, as shown in Fig. 2(d), was used as the input motion, which is the same as that used in the analysis of the lower San Fernando dam [9].

As shown in Fig. 2(b), the mesh is grouped into several subregions according to soil description. They are a zone of rolled fill (at the top of the dam), two zones of hydraulic fill (extended from both the upstream and downstream slopes), together with a clay core and two layers of alluvium (foundation).

While an extensive study on the lower San Fernando dam, including in situ testing as well as sampling and laboratory testing, was performed during the period 1985–1987 [11–13], the upper dam was not included in that investigation and, hence, no detailed information about the soils in the upper dam was reported. However, the upper and lower dams are located within about 3 km from each other. Both are founded on similar natural alluvial soils and, of most importance, both were constructed primarily by hydraulic filling method using similar borrow materials. The results of drilling, sampling, and trenching at both dams indicated no major difference in the type or quality of finished product between the two dams [14]. Therefore, it seems appropriate to deem the soil data for the lower dam applicable to the upper dam as well. Hence, the same constitutive model and model constants as used in the lower dam analyses were adopted for the upper dam analyses, so were the values of initial void ratio and the coefficients of permeability for each type of the soils [9].

5. Initial stress fields

The initial stress fields were established by performing static analyses with a gradually increasing gravitational acceleration from zero to g (9.81 m/s^2). Two such static analyses were performed for the upper San Fernando dam. One was with seepage forces acting on the soil by setting a water table of 15.3 m in height only in the upstream reservoir [Fig. 2(b)]. The other was without the seepage force by setting the same water table of 12.2 m in height on both the upstream and downstream sides under otherwise identical conditions [Fig. 2(c)]. This latter case is of course hypothetic and for comparison purpose only. The calculated fields of mean normal stress, p', in-plane shear stress, σ_{13}, and stress ratio, σ_{13}/p', as well as the directions and relative magnitudes of the seepage forces for the two cases, are shown in Figs. 3 and 4, respectively. It can be seen that, although the fields of the mean normal stress in the two cases are almost identical, the fields of the shear stress and the stress ratio are clearly different. With the seepage forces acting (Fig. 3), the neutral zone ($\sigma_{13}=0$) is shifted towards the upstream side, and the magnitudes of σ_{13} are significantly higher on the downstream side (compared with Fig. 4). It can also be seen clearly from Fig. 3(d) that the seepage forces tend to drive the soils towards the downstream direction once flow liquefaction occurs.

Two similar static analyses (one is for the original dam and the other is a hypothetical case with the same water
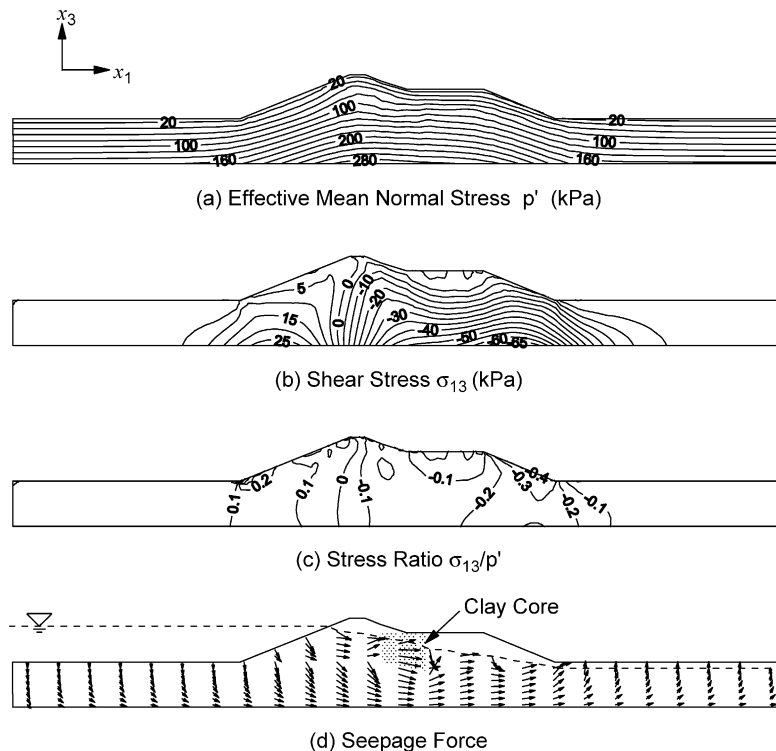

(a) Effective Mean Normal Stress p' (kPa)

(b) Shear Stress σ_{13} (kPa)

(c) Stress Ratio σ_{13}/p'

(d) Seepage Force

Fig. 3. Initial stress fields in the upper San Fernando dam (with seepage force).

x_3

x_1

(a) Effective Mean Normal Stress p' (kPa)

(b) Shear Stress σ_{13} (kPa)

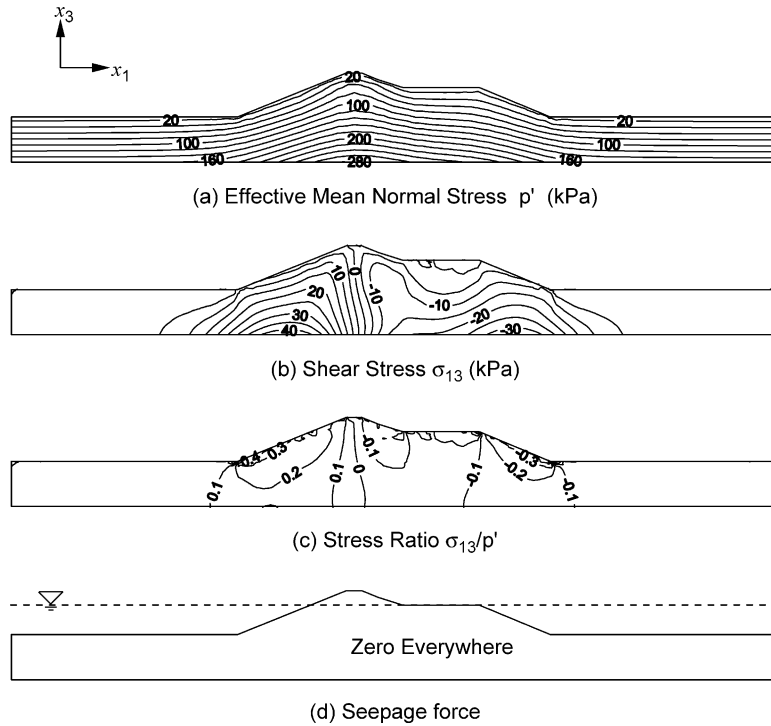(c) Stress Ratio σ_{13}/p'

Zero Everywhere

(d) Seepage force

Fig. 4. Initial stress fields in the upper San Fernando dam (without seepage force).

table on both the up- and down-stream sides) were performed for the lower San Fernando dam, too. The distributions of the in-plane shear stress and the seepage force in the two cases are shown in Fig. 5(a–d). While Fig. 5(a–d) show the same general trend as their counterparts in Figs. 3 and 4, the in-plane shear stresses in Fig. 5(a) and (c) (lower dam cases) are noticeably higher than those shown in Figs. 3(b) and 4(b) (upper dam cases), reflecting the difference in size between the two dams.

6. Analysis results of upper dam

6.1. Response with seepage force present

The computed deformed mesh at the end of the earth shaking ($t = 40$ s), together with the observed displacements

reported by Seed et al. [14,15], are shown in Fig. 6(a). A downstream movement is clearly seen from the deformed mesh. The computed and measured displacements match reasonably well.

Fig. 7(a) shows the calculated excess pore pressure, Δu_w, at $t = 6$ s, and Fig. 7(b) shows the corresponding excess pore pressure ratio in terms of $\Delta u_w/\sigma'_{v0}$, where σ'_{v0} is the initial effective vertical stress. The pore pressure ratio in the lower part of the hydraulic fill is quite high, indicating that soils in this region may have either liquefied or severely weakened. At both the upstream and downstream toe of the dam, the pore pressure ratio also goes up to or beyond 0.9, in agreement with the field observations of sandboils at the downstream toe. Fig. 8 shows the time histories of excess pore water pressure and effective mean normal stress at three representative locations, as indicated in Fig. 2(c). Point G968 [Fig. 8(a)] is in the alluvium layer

(a) In-Plane Shear Stress Contour (with seepage force)

In-Plane Shear Stress σ_{13} (kPa)

(b) Seepage Force Contour (with seepage force)

Seepage Force Direction and Intensity

(c) In-Plane Shear Stress Contour (without seepage force)

In-Plane Shear Stress σ_{13} (kPa)

(d) Seepage Force Contour (without seepage force)

Zero Everywhere

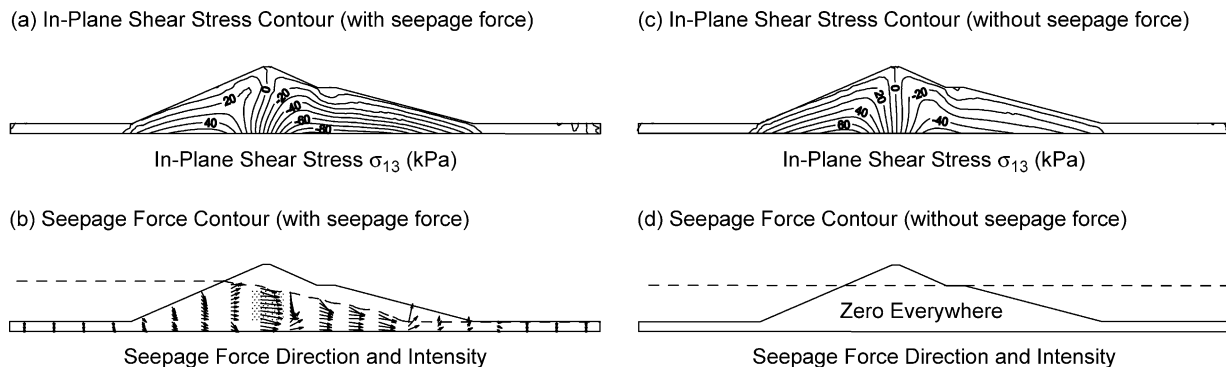Seepage Force Direction and Intensity

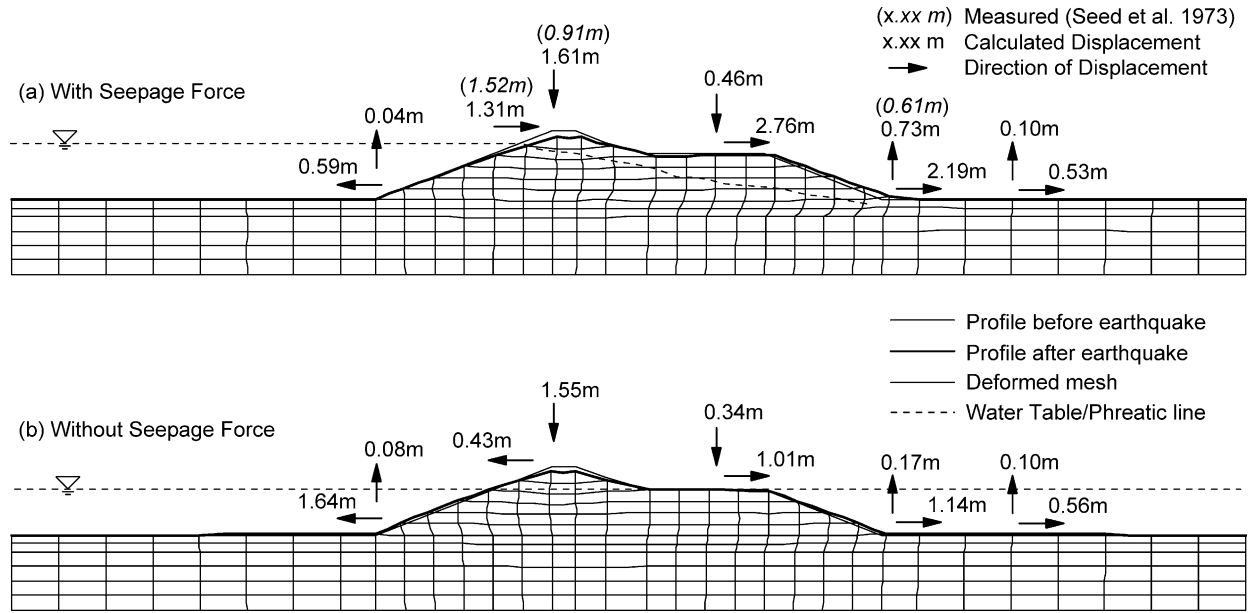Fig. 5. In-plane shear stresses and seepage forces in the lower San Fernando dam.

Fig. 6. Deformed meshes of the upper San Fernando dam. (a) With seepage force; (b) without seepage force.

close to the bottom of the dam foundation. Points G1022 [Fig. 8(b)] and G1535 [Fig. 8(c)] are located in the upstream and downstream hydraulic fill, respectively. The time histories show that pore pressures Δu_w start to increase and the effective mean normal stresses p' start to drop as the shaking starts. In Fig. 8(a) (alluvium, $e = 0.567$),

p' drops to a residual value higher than its counterparts in Fig. 8(b) and (c) (hydraulic fill, $e = 0.660$), reflecting the different steady state strengths resulting from the different soil densities. In the deeper layer, where G968 is located, the excess pore pressure starts to dissipate even during the earthquake.
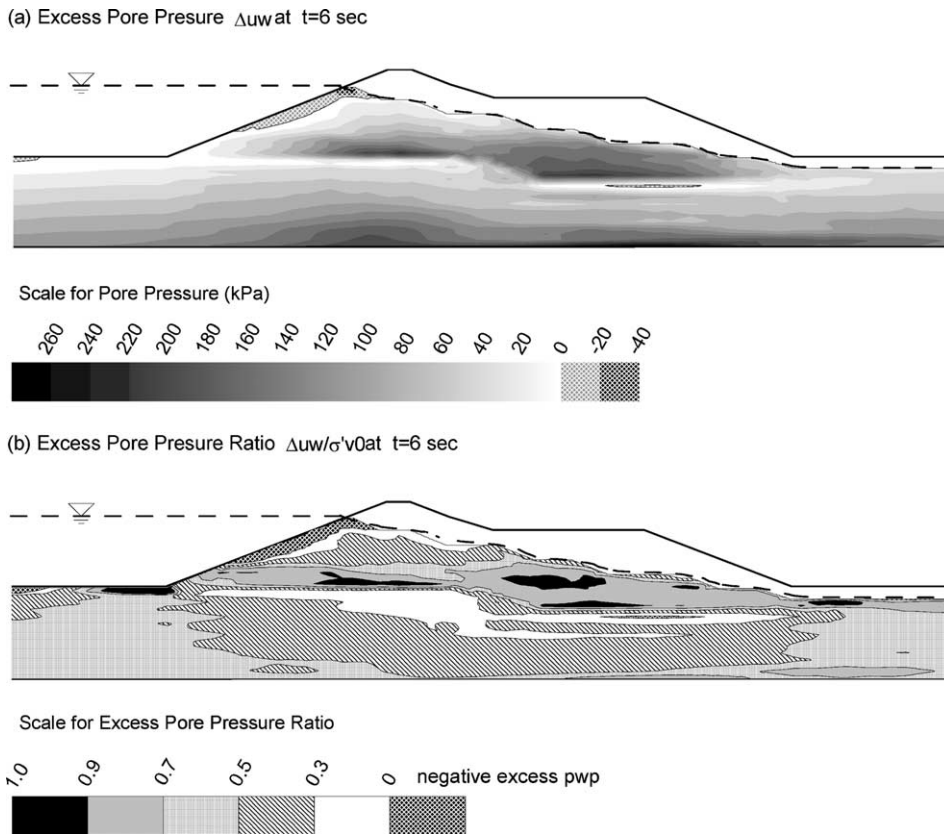

Fig. 7. Contours of excess pore pressure and pore pressure ratio of the upper San Fernando dam ($t = 6$ s).
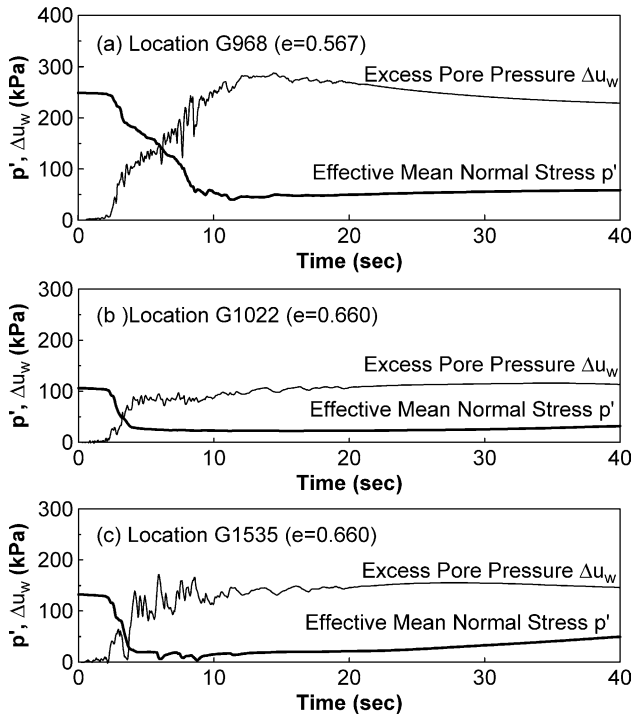
Fig. 8. Pore pressure and effective mean normal stress time histories at selected locations in the upper San Fernando dam.

Fig. 9 shows the calculated time histories of horizontal displacement at the crest and at the center of the downstream berm. The displacements are clearly biased towards the downstream direction, and the sliding rates (velocities) are higher between $t=3$ s and $t=10$ s, corresponding to the duration of strong shaking [refer to Fig. 2(d)]. The sliding rates gradually reduce afterwards, and at $t=40$ s, the slide nearly stops.

6.2. Response without seepage force present

This is a hypothetical case, where the seepage forces are eliminated by setting the same water table on both the upstream and downstream sides [Fig. 2(c)]. Other conditions are the same as in the previous analysis. By comparing Fig. 4 with Fig. 3, one can see that the seepage driving force has now totally disappeared; and
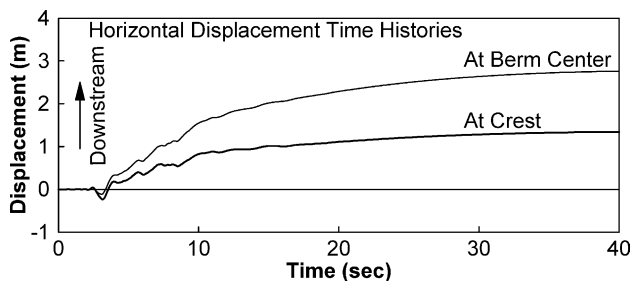

Fig. 9. Horizontal displacement time histories at representative locations in the upper San Fernando dam.

correspondingly, the static shear stress σ_{13} is distributed much more symmetrically in the embankment.

The deformed mesh at the end of the earthquake ($t=40$ s) is shown in Fig. 6(b). Compared with Fig. 6(a), where seepage forces are present and the whole dam moves downstream, one can see that without seepage forces, the upstream slope including the crest moves to the upstream side and the downstream slope including the downstream berm moves to the downstream side. The horizontal crest displacement is now 0.43 m to the upstream side, in contrast to the 1.31 m downstream displacement in Fig. 6(a). The horizontal displacement at the upstream toe is 1.64 m upstream, which is almost three times the value (0.59 m) in Fig. 6(a). The horizontal displacement at the downstream toe and the center of the downstream berm top is 1.14 and 1.01 m, respectively, which are far less than their counterparts (2.19 and 2.76 m) in Fig. 6(a). The vertical displacement at the downstream toe is 0.17 m (upward ridge), only one quarter of the value (0.73 m) in Fig. 6(a). Unlike the noticeable differences between Fig. 6(a) and (b) in terms of the lateral displacements and vertical displacement at the downstream toe, the settlements at the crest and at the center of downstream berm in the two cases are quite close.

It should be pointed out that raising the water table on the downstream side in this hypothetical case not only eliminates the seepage effect but also reduces the effective stress on the downstream side, which would in general increase the downstream deformation. In other words, if this side effect were not there, the downstream displacement would be even less, which in fact enhances the observation of the seepage driving effect.

It can be summarized that in the upper San Fernando dam case, the deformation pattern of the dam without seepage forces acting is noticeably different from that with seepage forces present. An overall downstream movement occurs when the seepage forces are present, whereas, with the seepage forces removed, the dam deforms evenly in both the upstream and downstream directions.

7. Analysis results of lower dam

7.1. Response with seepage force present

The detailed results of this case have been reported in Ming and Li [9]. For convenience of comparison with the case without seepage driving forces, the deformed mesh and selected time histories of horizontal displacement are replotted in Figs. 10(a) and 11(a), respectively.

7.2. Response without seepage force present

The computed deformed mesh at $t=40$ s in this case is shown in Fig. 10(b). While the overall pattern of deformation in the embankment is similar to that in
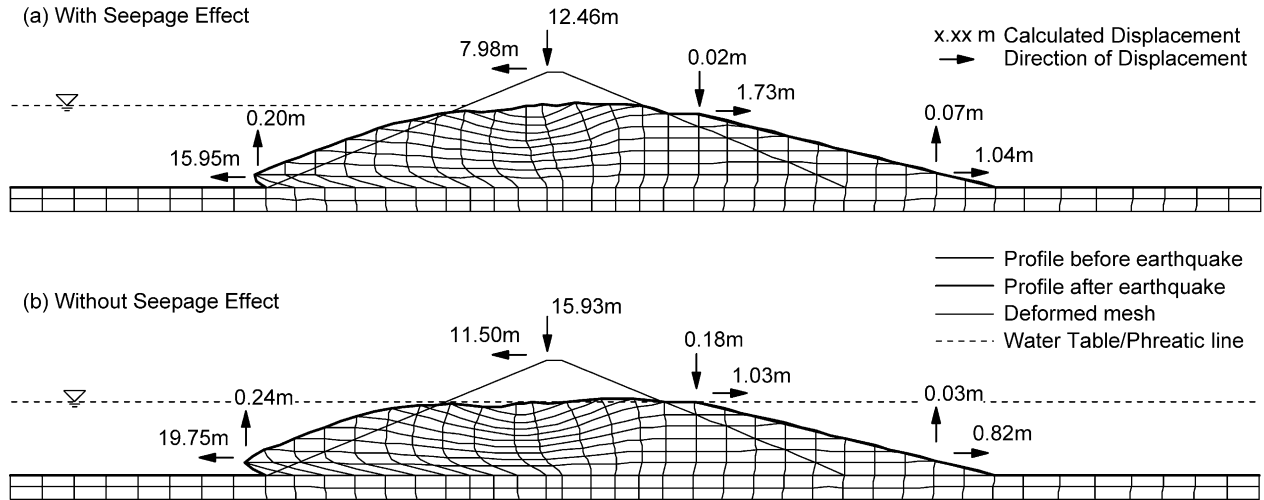
Fig. 10. Deformed meshes of the lower San Fernando dam. (a) With seepage force; (b) without seepage force.

Fig. 10(a), i.e. the upstream shell slides together with the crest into the reservoir and the downstream berm moves downstream slightly, the extent and rate of deformation in the two cases are noticeably different. Without the action of seepage forces, the upstream shell and the crest slide more to the reservoir (11.5 m vs. 8.0 m of lateral displacement at the crest), whereas the lateral displacements on the downstream side are slightly less. Compared with Fig. 10(a), the settlement at the crest in Fig. 10(b) (without seepage forces) is larger (15.9 m vs. 12.5 m) because of the larger upstream lateral displacement. Fig. 11(b) shows the time histories of horizontal displacement at the upstream toe, the crest, and the downstream berm, respectively. The calculated displacement rate at the upstream toe at $t = 40$ s is about 0.66 m/s, which is higher that its counterpart in the case with the seepage forces [0.38 m/s, as shown in Fig. 10(a)].

The overall patterns of the calculated deformations of the lower San Fernando dam with and without the presence of the seepage driving forces are similar. However, without the seepage forces in the downstream direction, the upstream shell and the crest move more towards the upstream direction and the downstream berm deforms less to the downstream direction.

8. Discussions

8.1. Difference in post-liquefaction displacement responses of upper and lower dams

It has been shown that for the upper San Fernando dam, the downstream seepage forces play an important role in driving the embankment towards downstream direction upon liquefaction. Fig. 12(a) and (b) show the displacement vector fields of the upper San Fernando dam in the cases with and without seepage forces. It can be seen that in the case with seepage forces present [Fig. 12(a)] the displacements of the dam are downstream overall, whereas, in

the case in which the seepage forces are absent [Fig. 12(b)], the displacements are much less biased. Fig. 12(c) shows the difference in displacement vectors between the two cases. A comparison of the differential displacement vector field [Fig. 12(c)] with the vector field of the seepage force intensity [Fig. 12(d)] shows that the two vector fields correlate with each other quite well, indicating clearly the influence of the seepage force on the deformation of the dam. On the downstream side above the phreatic line, seepage is absent but displacement is large, reflecting the controlling rigid body motion in that zone.

One may gain more insights into the different lateral displacement responses by examining Fig. 13(a), which shows the distributions of the driving shear stress and the residual strengths of the soil (hydraulic fill materials) along the base of the embankment (the bottom boundaries of
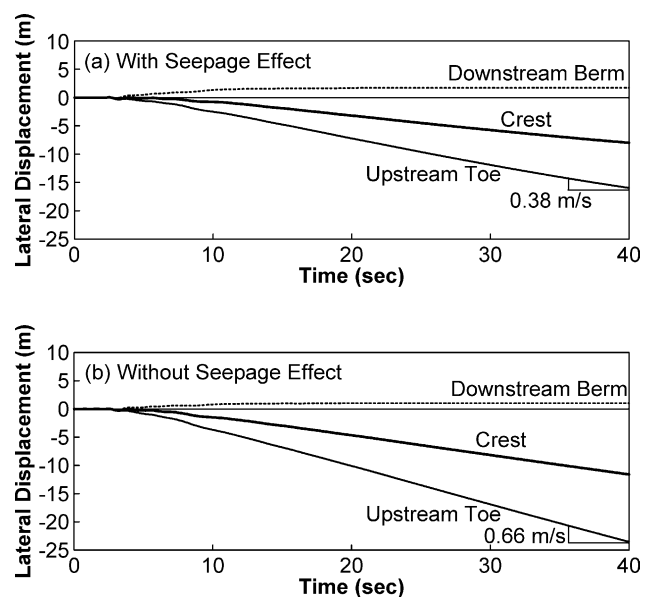

Fig. 11. Horizontal displacement time histories at representative locations in the lower San Fernando dam.

(a) Displacement Field (with seepage forces)

(b) Displacement Field (without seepage forces)

(c) Difference of Two Displacement Fields ((a)-(b))
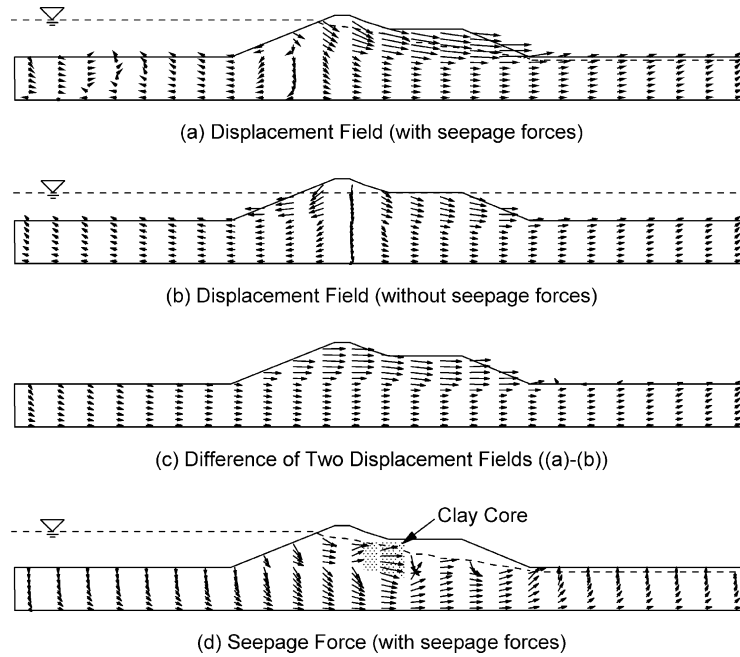
(d) Seepage Force (with seepage forces)

Fig. 12. Displacement vector fields with and without seepage force acting (upper San Fernando dam).

the hydraulic fill zones) of the upper dam, where, based on the calculated results, the soil is likely to experience severe shear deformations. The figure shows that, with seepage present, the static driving forces are higher than the residual strength of the soil only on the downstream side, indicating that only the downstream soil may produce flow type displacement when liquefaction is triggered. As a result, upon liquefaction, the dam moves towards the downstream
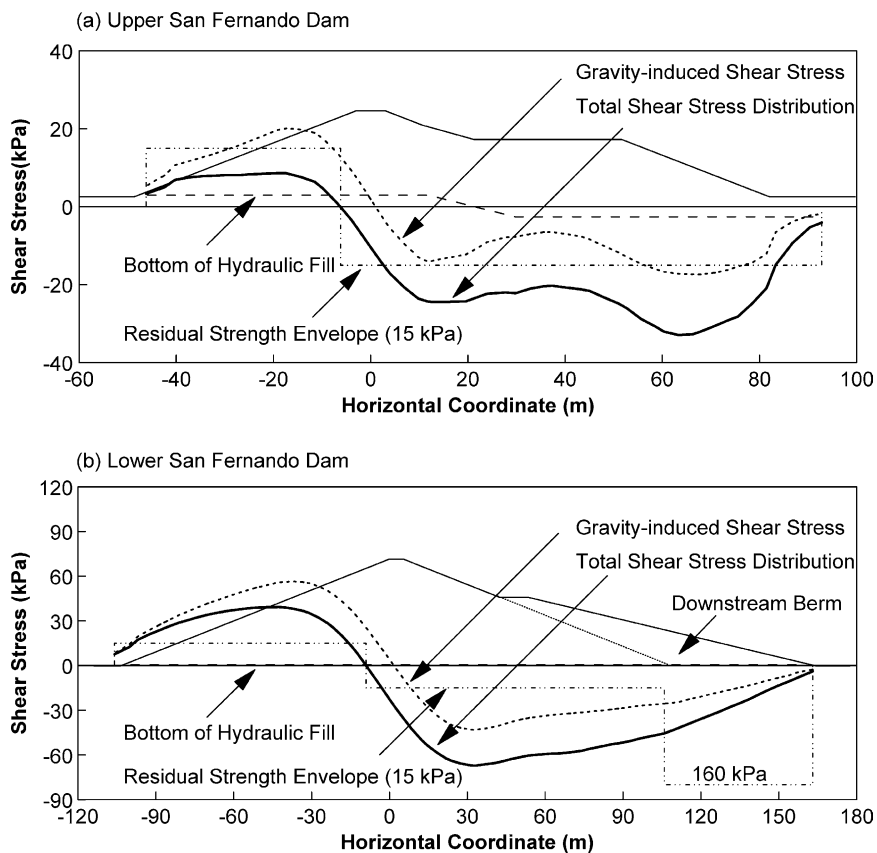

Fig. 13. Driving shear stress and residual strength envelopes along the bottom of the embankment. (a) Upper San Fernando dam; (b) lower San Fernando dam.

direction. On the other hand, when the seepage forces are removed, leaving only the driving forces caused by gravity, the upstream driving shear stresses exceed the residual strength of the soil only marginally and only in a confined zone, and the downstream driving stresses are reduced to be mostly within the residual strength envelope. As a result, the dam would deform quite evenly in both the upstream and downstream directions.

Compared with the upper dam, however, the seepage driving effect has not altered the overall deformation pattern of the lower dam drastically. This may be explained by examining Fig. 13(b), the counterpart of Fig. 13(a) for the lower dam. It can be seen that while the residual strengths of the soils at the embankment base (hydraulic fill materials) in the two figures are the same ($\sim$15 kPa), the driving shear stresses are very different, due to the differences between the two dams in size and configuration. Furthermore, the residual strength envelope in Fig. 13(b) includes a high strength segment ($\sim$160 kPa) that matches the alluvial material below the downstream berm.

Referring to Fig. 13(b), one can see that on the upstream side of the lower dam, the shear stresses are significantly higher than the residual strength of the soil (hydraulic fill), no matter whether the seepage driving force is present. Once a sufficient amount of soil in the lower part of the upstream slope liquefies, in both cases (with and without the seepage effect) the upstream flow slide starts to develop. Since the shear stresses there are higher in the case without the seepage forces, the extent of upstream flow deformation as well as its rate is also higher. On the downstream side, the magnitudes of the static shear stresses, although significantly higher than the residual strength of the hydraulic fill material, are far less than the strength of the alluvial material ($\sim$160 kPa) below the downstream berm. This observation is applicable to both the cases, either with or without the seepage driving effect. As a result, no flow

liquefaction occurs in the lower part of the downstream berm and its foundation, and, consequently, the berm provides an effective support to the soils in the downstream slope, which themselves may have already liquefied or weakened during the earthquake. For the part of soils that have liquefied but do not show notable flow deformation, the situation is somewhat like a strain-controlled test on a softening material, in which the development of the post-peak strain is constrained by the external kinematic conditions.

8.2. Effectiveness of densification of liquefiable soils in upper dam

As shown in Fig. 13(a), due to the seepage effect, the static shear stresses at the embankment base of the upper San Fernando dam exceed the residual strength of the soil on the downstream side, whereas they are lower than the residual strength of the soil on the upstream side. In order to reduce the downstream movement of the embankment during a strong earthquake, it would be most effective to improve the residual strength of the soil only on the downstream side. Fig. 14(a) shows the deformed mesh of the upper dam with the density of the lower part of the downstream hydraulic fill (shaded area) increased from $e = 0.660$ to $e = 0.620$ (residual strength from 15 to 50 kPa). Compared with the case without local densification the deformation as well as the downstream movement of the dam is reduced significantly. Fig. 14(b) shows the deformed mesh of the dam with a similar densification but on the upstream side (shaded area). Compared with the original dam (without densification), the overall improvement of the dam performance is insignificant in this case. The results shown in Fig. 14(a) and (b) suggest that the seepage driving effect is significant only when significant seepage forces appear in liquefiable soil, and an efficient way to reduce this
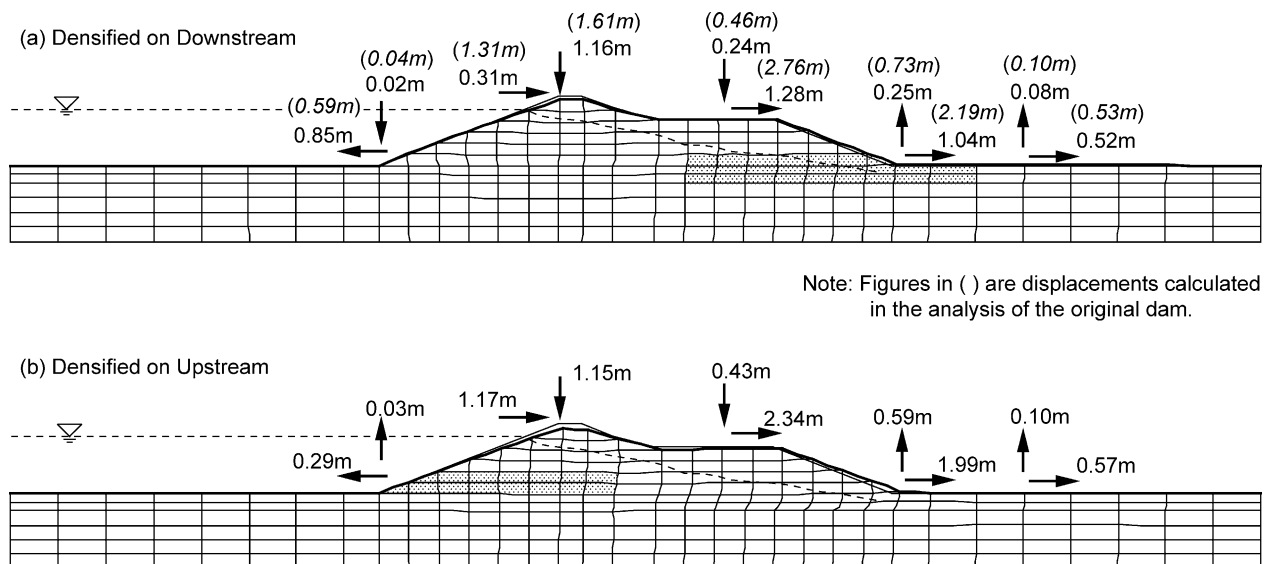

Fig. 14. Deformed meshes of the upper San Fernando dam after local densification of the liquefiable soil. (a) On the downstream side; (b) on the upstream side.

effect is to improve the soil only in the region where the driving stress exceeds the residual strength of the soil.

8.3. Stress–strain responses of soils

As shown before, the main effect of seepage during an earthquake is its role as a driving force acting on the soil skeleton that pushes soil away when flow liquefaction is triggered. This flow deformation mechanism is evident in the local soil responses. Here only the upper dam is used as example. Fig. 15(a–f) show the stress paths and the shear stress–strain responses of the soil at location G1022 [refer to Fig. 2(c) for the location], which is in the loose hydraulic fill and has an initial σ_{13} of -8.0 kPa when seepage forces are present and an initial σ_{13} of 0.8 kPa when seepage forces are removed. This initial σ_{13} acts as a static driving stress that affects the motion of the soil at that location after liquefaction is triggered. At the end of the earthquake ($t=$ 40 s), the shear strains, γ_{13}, in the two cases are -11.1% and $+0.74\%$, respectively. The p'–q stress paths (here $q=\sqrt{3J_{2D}}$ is a deviatoric stress invariant representing the magnitude of all shear components and is compatible with its definition in the triaxial space) in the two cases are shown in Fig. 15(c) and (f), respectively. Because the deviatoric component attributed to the differences between the vertical and lateral normal stresses predominates q, and this deviatoric component is not significantly affected by the presence of seepage force and produces merely unbiased shear deformation, the two paths in Fig. 15(c) and (f) are very similar. It can be seen from these plots that flow

liquefaction has indeed been triggered and a residual strength (in terms of q) of around 25 kPa is observed.

Fig. 16(a–f) show the soil responses at G1535 [refer to Fig. 2(c)], which is located near the bottom of the downstream hydraulic fill. The responses at this location show that the deviatoric stress, q, gradually reduces as shear deformation develops [16] so that the mean effective normal stress, p', can reach a very low value. In both the cases (with and without seepage effect), one can see some cyclic mobility response when p' becomes low. With the seepage induced driving force, a very large shear strain (-37.6%) is developed at the end of the earthquake [Fig. 16(b)], whereas, without this driving force, the mean effective normal stress p' approaches zero [Fig. 16(d) and (f)], accompanying a large, but limited, shear strain (-12%) [Fig. 16(e)]. The latter case is similar to the response in level ground.

Fig. 17(a–f) show the soil responses at location G968 [refer to Fig. 2(c)], which is located in the embankment foundation, i.e. in the alluvium layer. Because of a relatively high density ($e=0.567$ in the analyses), flow type deformation does not occur, and the shear strains are limited. However, one can still see the influence of the seepage force. As shown in the figures, this location has an initial σ_{13} of -16.1 kPa when seepage forces are present and an initial σ_{13} of $+7.6$ kPa when seepage forces are removed. Even though flow liquefaction did not happen, this static σ_{13} still yields a biased shear deformation following the static shear direction. At the end of the earthquake, the shear strains in the two cases took opposite signs: -1.85% with seepage force and $+0.38\%$ without.
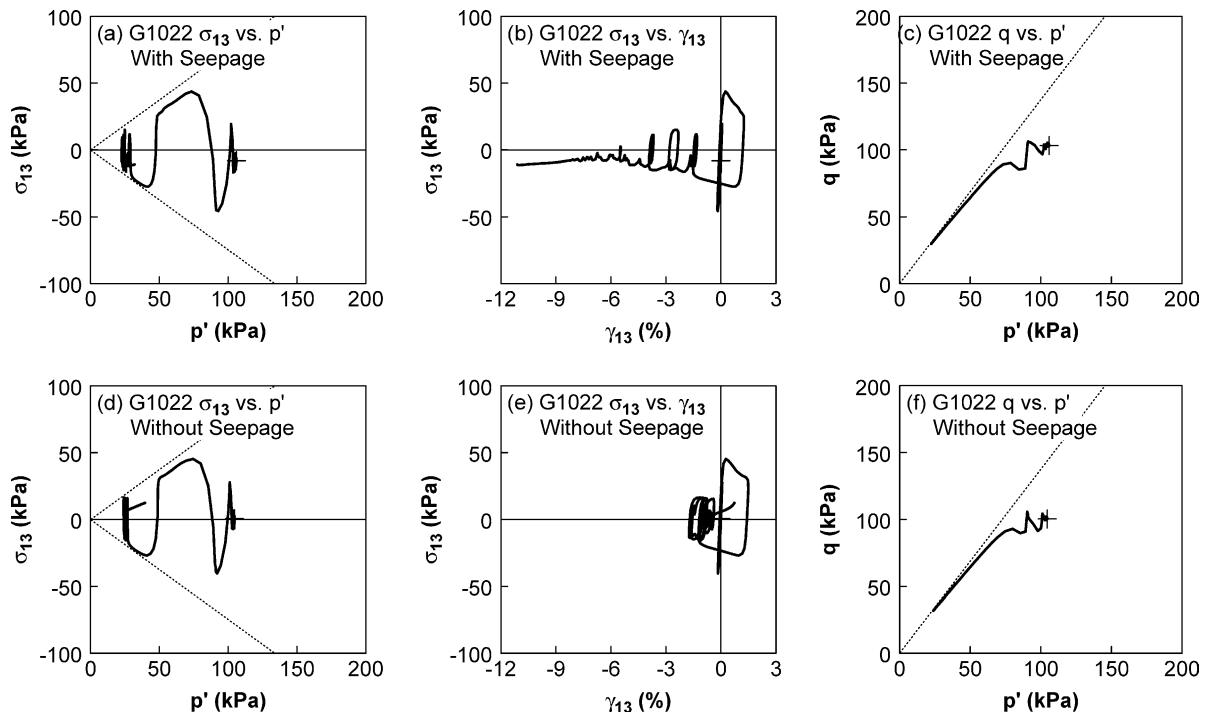

Fig. 15. Stress paths and stress–strain relationships at location G1022 (upper San Fernando dam).
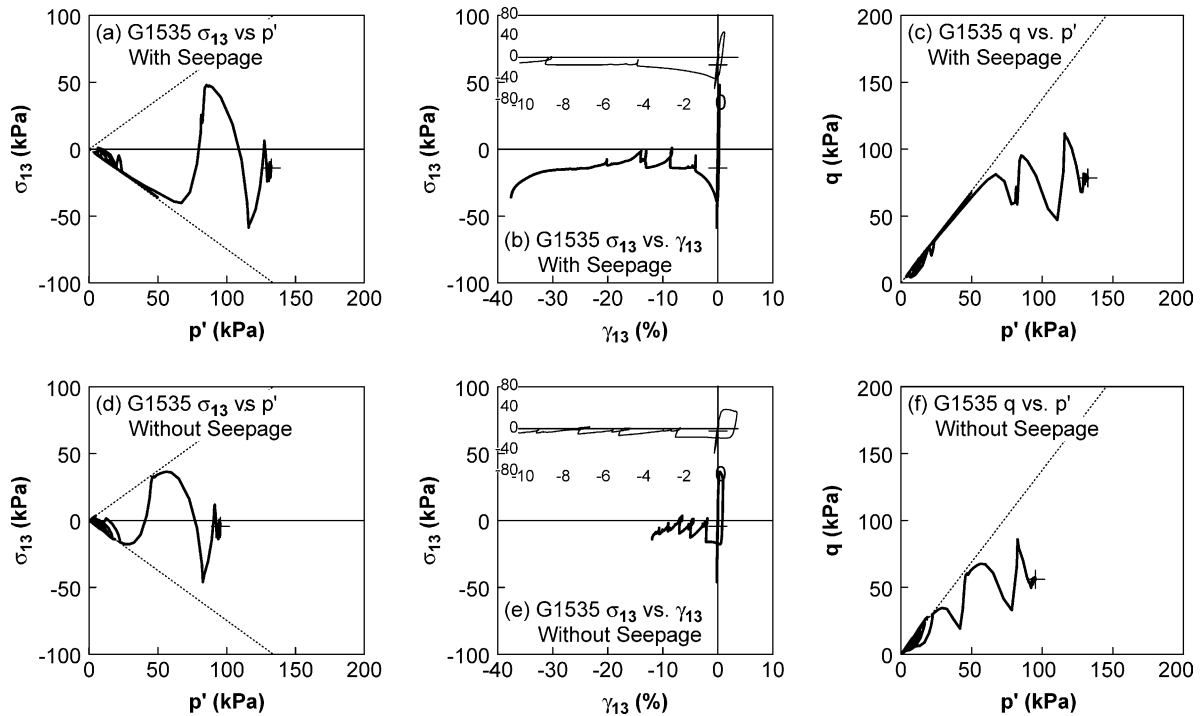
Fig. 16. Stress paths and stress–strain relationships at location G1535 (upper San Fernando dam).

8.4. Acceleration responses

Fig. 18(a–c) show the calculated acceleration responses at three different elevations. Their locations, N480, N472, and N460, are indicated in Fig. 2(c). N480 is at the crest while N472 and N460 are located in the hydraulic fill and the alluvium layer, respectively. The input accelerogram is

shown as well in Fig. 18(d). The acceleration response at point N472 (in the hydraulic fill) is very different from the others. The development of a very high excess pore water pressure in the hydraulic fill results in such a low shear stiffness that the acceleration amplitude is significantly reduced and the high-frequency components are mostly damped out. It is not difficult to identify that liquefaction
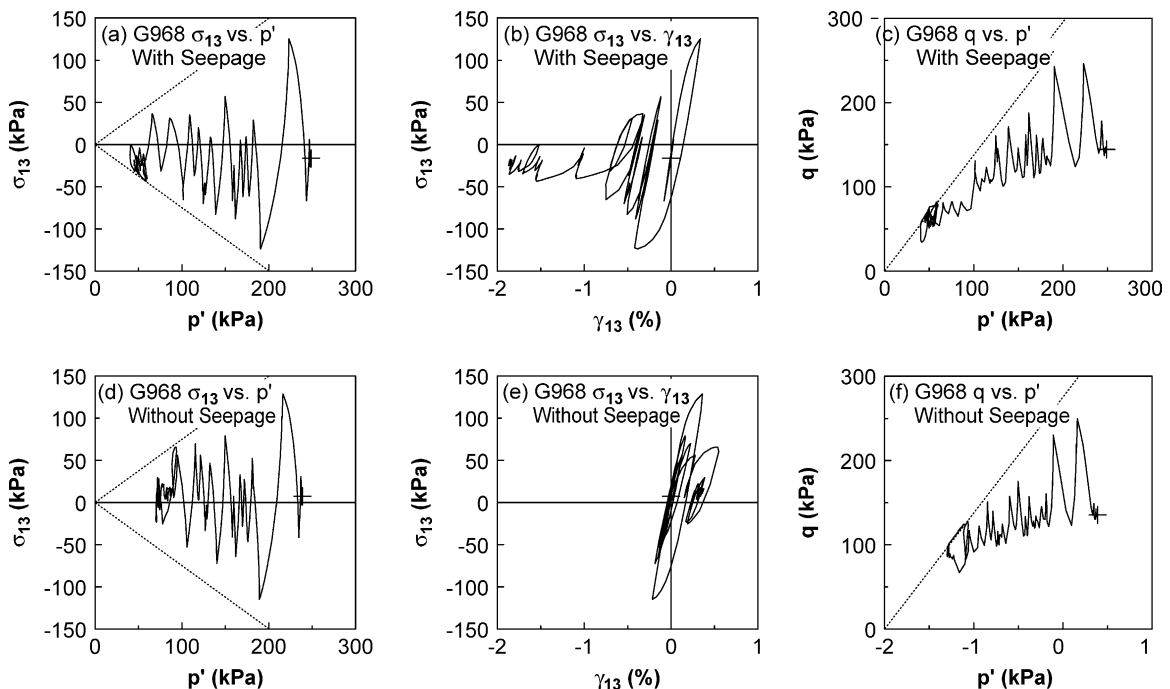

Fig. 17. Stress paths and stress–strain relationships at location G968 (upper San Fernando dam).
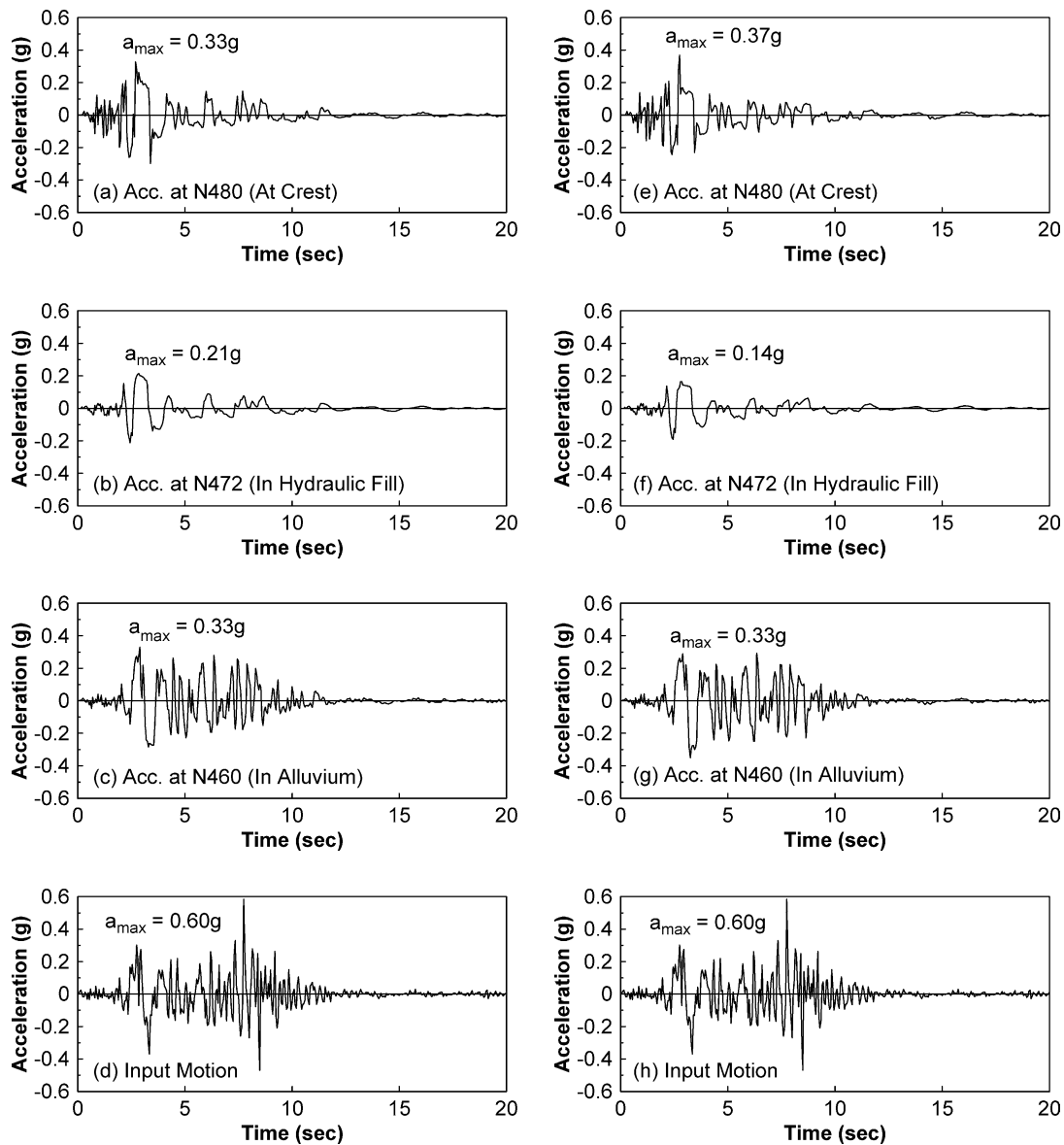
Fig. 18. Acceleration time histories at three different elevations (N460, N472, and N480) in the upper San Fernando dam.

occurs in the hydraulic fill. N480 [Fig. 18(a)] is located above the phreatic line, where the soil is dry. Compared with N472 [Fig. 18(b)], the acceleration at N480 is amplified to a certain extent. Fig. 18(e–g), the counterpart of Fig. 18(a–c) show the acceleration responses of the same locations without seepage forces acting. The acceleration time histories in the two cases are quite similar, indicating that the acceleration response is not sensitive to the presence of seepage force.

9. Conclusions

Evaluation of post-liquefaction flow deformation as well as the resulting displacement is now a central part in design and remediation of earth dams in seismically active regions.

This is especially true when the deformations and displacements are significant but still restricted (i.e. the dam is not completely collapsed), because they are still manageable at an acceptable cost. The issue then becomes how to adequately quantify the deformations and displacements in this category.

Post-liquefaction flow deformations and displacements are sensitive to both the residual strength of the soil and the driving stress acting on it. While numerous investigations on determining the residual strength have been performed during the past 20 years, no parallel attention has been paid to the accuracy of the determination of driving forces.

This paper draws attention to the driving effect of the seepage force, which is a force that tends to drive soils away from their in situ positions when liquefaction is triggered. This seepage driving effect is significant if (i) it is

comparable to that of the gravitational driving forces; (ii) it is present in loose liquefiable soils; and (iii) the deformations of the liquefied soils are not confined by non-liquefiable soils. The analyses presented in this paper show that the seepage driving effect is significant in the upper San Fernando dam case, in which all the above conditions are met, but less pronounced (in a relative term) in the lower San Fernando dam case, in which the conditions (i) and (iii) are not met.

As the configuration and soil profile of an earth dam could be quite complicated, fully coupled analyses are recommended for evaluating the seepage as well as other effects. For a fully coupled procedure for liquefaction analysis, it is cardinally important to have a constitutive model that is capable of realistically describing the granular soil behavior over the full range of loading conditions encountered during an earthquake.

Acknowledgements

References

[1] Serff N, Seed HB, Makdisi FI, Chang CY. Earthquake induced deformations of earth dams. Rep. No. EERC 76-4, Earthquake Engineering Research Center, University of California, Berkeley, CA, 1976.

[2] Seed HB. Consideration in the earthquake-resistant design of earth and rockfill dams. Géotechnique 1979;29(3):215–63.

[3] Biot MA. General theory of three dimensional consolidation. Journal of Applied Physics 1941;12:155–64.

[4] Biot MA. Theory of elasticity and consolidation for a porous anisotropic solid. Journal of Applied Physics 1955;26(2):182–5.

[5] Zienkiewicz OC, Shiomi T. Dynamic behavior of saturated porous media: the generalized Biot formulation and its numerical solution. International Journal for Numerical and Analytical Methods in Geomechanics 1984;8:71–96.

[6] Ming HY. Fully-coupled earthquake response analysis of earth dams using a critical state sand model. PhD Thesis, Hong Kong University of Science and Technology, Hong Kong, China 2001.

[7] Li XS. A sand model with state-dependent dilatancy. Géotechnique 2002;52(3):173–86.

[8] Li XS, Dafalias YF. Dilatancy for cohesionless soils. Géotechnique 2000;50(4):449–60.

[9] Ming HY, Li XS. Fully coupled analysis of failure and remediation of lower San Fernando dam. Journal of Geotechnical and Geoenvironmental Engineering, ASCE 2003;129(4):336–49.

[10] CSMIP. (http://docinet3.consrv.ca.gov/csmip), Strong Motion Instrumentation Program, Division of Mines and Geology, Department of Conservation, California, 1999.

[11] Castro G, Keller TO, Boynton SS. Re-evaluation of the lower San Fernando Dam. Report 1: an investigation of the February 9, 1971 slide Contract report GL-89-2. Washington, DC: US Army corps of Engineers; 1989.

[12] Castro G, Seed RB, Keller TO, Seed HB. Steady-state strength analysis of lower San Fernando dam slide. Journal of Geotechnical Engineering, ASCE 1990;118(3):406–27.

[13] Seed HB, Seed RB, Harder LF, Jong HL. Re-evaluation of the Lower San Fernando Dam. Report 2, Examination of the post-earthquake slide of February 9, 1971 Contract Report GL-89-2. Washington, DC: US Army corps of Engineers; 1989.

[14] Seed HB, Lee KL, Idriss IM, Makdisi F. Analysis of the slides in the San Fernando dams during the earthquake of February 9, 1971 Report No. EERC 73-2. Berkeley: University of California; 1973.

[15] Seed HB, Lee KL, Idriss IM, Makdisi FI. The slides in the San Fernando dam during the earthquake of February 9, 1971. Journal of Geotechnical Engineering Division, ASCE 1975; 101(GT7):651–88.

[16] Li XS. Rotational shear effects on ground earthquake response. Soil Dynamics and Earthquake Engineering 1997;16(1):9–19.